



The optimal ^{18}F -fluoromisonidazole PET threshold to define tumor hypoxia in preclinical squamous cell carcinomas using pO_2 electron paramagnetic resonance imaging as reference truth

Inna Gertsenshteyn^{1,2,3} · Boris Epel^{2,3} · Amandeep Ahluwalia¹ · Heejong Kim¹ · Xiaobing Fan^{1,4} · Eugene Barth^{2,3} · Marta Zamora^{1,4} · Erica Markiewicz⁴ · Hsiu-Ming Tsai⁴ · Subramanian Sundramoorthy^{2,3} · Lara Leoni⁴ · John Lukens^{2,3} · Mohammed Bhuiyan¹ · Richard Freifelder¹ · Anna Kucharski¹ · Mihai Giurcanu⁵ · Brian B. Roman^{1,4} · Gregory Karczmar^{1,4} · Chien-Min Kao^{1,4} · Howard Halpern^{2,3} · Chin-Tu Chen^{1,4} 

Received: 3 March 2022 / Accepted: 19 June 2022

© The Author(s), under exclusive licence to Springer-Verlag GmbH Germany, part of Springer Nature 2022

Abstract

Purpose To identify the optimal threshold in ^{18}F -fluoromisonidazole (FMISO) PET images to accurately locate tumor hypoxia by using electron paramagnetic resonance imaging (pO_2 EPRI) as ground truth for hypoxia, defined by $\text{pO}_2 \leq 10$ mmHg.

Methods Tumor hypoxia images in mouse models of SCCVII squamous cell carcinoma ($n = 16$) were acquired in a hybrid PET/EPRI imaging system 2 h post-injection of FMISO. T2-weighted MRI was used to delineate tumor and muscle tissue. Dynamic contrast enhanced (DCE) MRI parametric images of K^{trans} and v_e were generated to model tumor vascular properties. Images from PET/EPRI/MRI were co-registered and resampled to isotropic 0.5 mm voxel resolution for analysis. PET images were converted to standardized uptake value (SUV) and tumor-to-muscle ratio (TMR) units. FMISO uptake thresholds were evaluated using receiver operating characteristic (ROC) curve analysis to find the optimal FMISO threshold and unit with maximum overall hypoxia similarity (OHS) with pO_2 EPRI, where $\text{OHS} = 1$ shows perfect overlap and $\text{OHS} = 0$ shows no overlap. The means of dice similarity coefficient, normalized Hausdorff distance, and accuracy were used to define the OHS. Monotonic relationships between EPRI/PET/DCE-MRI were evaluated with the Spearman correlation coefficient (ρ) to quantify association of vasculature on hypoxia imaged with both FMISO PET and pO_2 EPRI.

Results FMISO PET thresholds to define hypoxia with maximum OHS (both $\text{OHS} = 0.728 \pm 0.2$) were $\text{SUV} \geq 1.4 \times \text{SUV}_{\text{mean}}$ and $\text{SUV} \geq 0.6 \times \text{SUV}_{\text{max}}$. Weak-to-moderate correlations ($|\rho| < 0.70$) were observed between PET/EPRI hypoxia images with vascular permeability (K^{trans}) or fractional extracellular-extravascular space (v_e) from DCE-MRI.

Conclusion This is the first *in vivo* comparison of FMISO uptake with pO_2 EPRI to identify the optimal FMISO threshold to define tumor hypoxia, which may successfully direct hypoxic tumor boosts in patients, thereby enhancing tumor control.

Keywords Tumor hypoxia · FMISO PET · EPRI · DCE-MRI

Introduction

Hypoxic tumors are generally associated with poor patient prognosis due to their resistance to radiation and chemotherapy [1–4]. Within solid tumors, hypoxia can induce

This article is part of the Topical Collection on Preclinical Imaging.

✉ Chin-Tu Chen
cchen3@uchicago.edu

¹ Department of Radiology, The University of Chicago, Chicago, IL, USA

² Department of Radiation and Cellular Oncology, The University of Chicago, Chicago, IL, USA

³ Center for EPR Imaging In Vivo Physiology, The University of Chicago, Chicago, IL, USA

⁴ Integrated Small Animal Imaging Research Resource, OSRF, The University of Chicago, Chicago, IL, USA

⁵ Department of Public Health Sciences, The University of Chicago, Chicago, IL, USA

several complex cellular processes triggered by expression levels of multiple protein responses, most notably the hypoxia inducible factor 1α , HIF- 1α [5]. This leads to increased and chaotic blood vessel formation (angiogenesis), metastasis, and aggressiveness of the cancer [6]. While the topic of low oxygenation and radiation sensitivity has been understood for eleven decades [7–9], there is still no widely accepted method for accurate *in vivo* hypoxia imaging that is in clinical use to better target tumor hypoxia.

In a preclinical setting, pulse electron paramagnetic resonance imaging (EPRI) is an accurate modality for measuring and imaging near-absolute pO_2 for oxygen-guided radiation therapy [4]. EPRI takes advantage of molecular oxygen's unpaired electrons and introduces an oxygen-sensitive spin probe into the system. The spin lattice relaxation rate of the probe's unpaired electron spin has a strong linear relationship with surrounding pO_2 with very little confounding variation [10]. Ongoing EPRI studies have demonstrated significant enhancement of tumor control by comparing a radiation boost to hypoxic tumor subregions with that of well oxygenated tumor subregions in several preclinical models [4]. This hypoxia dose painting method benefits subjects by minimizing dose to surrounding oxygenated tumor regions and organs at risk. Although results are promising, EPRI is not *yet* available for clinical use [11]. Therefore, in this study, EPRI is used as the ground truth hypoxia to evaluate a more clinically relevant hypoxic marker: ^{18}F -fluoromisonidazole (FMISO) PET.

FMISO PET is the most widely accessible hypoxia radiotracer for clinical studies [12, 13]. One clinical study (Vera et al. [14]) used FMISO PET to identify and treat tumor hypoxia for boost dose escalation. There was no evidence of benefit, but also no evidence of higher toxicity to organs at risk when delivering a boost to hypoxic tumor subregions; this is a promising result for dose painting. The head and neck cancer group at Memorial Sloan Kettering Cancer Center used FMISO PET to distinguish normoxic tumors for dose de-escalation [15], with remarkable evidence of tumor control at radiation doses with very mild side effect profiles. However, there is a lack of unanimous definition of tumor hypoxia across research groups, even within the same tumor type, leading to a variation in tumor hypoxia definition [16].

For example, in Vera et al. [14], tumor hypoxia was defined by voxel values with standardized uptake value (SUV) greater than 1.4; in Riaz et al. [15], tumor hypoxia was defined by tumor-to-muscle ratio (TMR) greater than 1.2. In a review on oxygen-guided radiotherapy outcomes by Ferini et al. [17], each study listed in Table 2 of the article used a different or unspecified method to define hypoxia with FMISO PET. Lindblom et al. [18] used a threshold of 1.4 times SUV_{mean} ; Cheng et al. [19] used a

threshold of tumor to muscle SUV ratio greater than 1.5; Henriques de Figueiredo [20] used the fuzzy logic based locally adaptive Bayesian method; Hendrickson et al. [21] did not specify the threshold used to define the hypoxic target volume. Inconsistent definitions of tumor hypoxia using FMISO PET can potentially have negative effects on patient survival and post treatment quality of life by over- or under-estimating hypoxic volumes.

The research presented here addresses the uncertainty in defining hypoxia with FMISO PET among research groups, using *in vivo* pO_2 EPRI as the ground truth hypoxia. The temporal variability of hypoxia, or acute hypoxia [22], has led to the development of an in-house imaging system of a hybrid PET/EPRI machine for near-simultaneous hypoxia imaging [23]. This has the advantage of imaging tumor hypoxia in two modalities while the mouse remains in the same position and physiological conditions, avoiding confounding effects and registration issues that are often present in multi-modal studies.

SCCVII squamous cell carcinoma mouse models were used to image tumor hypoxia with FMISO PET and pO_2 EPRI to identify the optimal FMISO uptake threshold in locating hypoxia. T2-weighted MRI was used to define tumor margins. Dynamic contrast enhanced (DCE-) MRI parametric images of K^{trans} and v_e were used to model the chaotic tumor vascular properties that are often associated with hypoxia. Immunohistochemical (IHC) stains of HIF- 1α expression were used to validate *in vivo* hypoxia images, and cluster of differentiation 31 (CD31) stains of endothelial cells were used to validate K^{trans} and v_e . Hematoxylin and Eosin (H&E) staining was used to identify necrosis.

Materials and methods

Animal tumor model

SCCVII squamous cell carcinoma tumors ($n=20$) were grown in the calf muscle of C3H female mice to mean volumes of $320 \pm 100 \text{ mm}^3$ within 12 days of tumor cell inoculation for imaging. Mice were 8–13 weeks old at the time of imaging. Four mice died before imaging was completed; therefore, 16 mice were included in analysis. The study has been approved by the Institutional Animal Care and Use Committee and followed US Public Health Service policy.

Image acquisition

A schematic of the imaging experiment is shown in Supplemental Figure S1. Hypoxia images were acquired in the hybrid PET/EPRI machine [23], and MR images were acquired in a 9.4 Tesla small animal scanner (Bruker,

Erlangen, Germany). During image acquisition, mice lay prone with anesthesia administered via nose cone maintained near 1.2% isoflurane. Mice were monitored to regulate their temperature at 37 ° C and respiratory rate near 100 bpm. Mice were not disturbed during imaging except for the disconnection of distant catheter access tubes.

Following induction of anesthesia using 2% isoflurane mixed with air, the tumor-bearing leg was immobilized in a soft vinyl polysiloxane cast (GC America, Alsip, IL) and plastic bed using a previously published methodology [24]. A tail vein cannula was inserted to administer a bolus injection of ~8.5 MBq of FMISO (produced on-site [25] and detailed in a previous publication [26]) for PET imaging. An infusion of oxygen-sensitive spin probe (OX071; GE Healthcare) was used for EPRI and a bolus of gadodiamide (Omniscan; GE Healthcare) for DCE-MRI.

For EPRI, spin-probe infusion began 1.5 h post-injection of FMISO. At least three pO_2 images were acquired at 7 min each; the last image was used for analysis to be temporally near the FMISO PET image. PET/EPRI were not acquired simultaneously due to RF-frequency interference. Immediately after EPRI imaging, a static 20–30-min PET image was acquired 2 h post-injection. Thirty minutes later, after the mouse was transferred to the MRI facility, T2-weighted (T2w) and DCE-MRI images were acquired. K^{trans} and v_e parametric images were generated using the Tofts model [27] described in detail in a previous publication [26].

To prepare tumors ($n=2$) for IHC staining, the tumor-bearing mouse leg was skinned and cut in half axially at the tumor center, and the leg was separated and dropped into formalin for 36 h. The leg was then transferred into decalcification solution for 2 h, after which the tumor (including surrounding muscle and decalcified bone to aid in registration with MRI images) was cut into two 5-mm axial sections at the center and set in labeled cassettes. The solution was rinsed with dewater and transferred into 70% ethanol for 24–36 h.

Four serial paraffin sections were prepared with 5-mm thickness every 500 μ m for multiparametric immunohistochemistry stained for H&E, CD31 (1:200 dilution; ab28364, Abcam), and HIF-1 α (1:1000 dilution; #NB100-479SS, Novus Biologicals). H&E was used to identify tumor vs healthy tissue cells and necrosis; CD31 targeted the endothelial cells of blood vessels to identify angiogenesis; and the HIF-1 α antibody was hypothesized to be expressed largely in tumor cells around necrosis and angiogenesis. This resulted in 16 potential slices for multiparametric IHC analysis.

Image analysis

Pre-processing

EPRI/PET/MRI images were registered and resampled to 0.5-mm isotropic voxels—the output voxel resolution of

PET images—using an in-house software [28] developed in MATLAB (MathWorks, Natick, MA). Anatomic landmarks and fiducials filled with water and the EPRI spin probe embedded in the plastic bed were used for registration.

The tumor was manually contoured in the axial slices of T2w MR images (Fig. 1). A small region of interest (ROI) was drawn in the muscle of the tumor-bearing leg near the femur to generate FMISO images in units of tumor-to-muscle ratio (TMR). Standardized uptake value (SUV) images were generated by normalizing the PET image concentration by the injected dose and mouse body weight. The tumor contour was transformed to all EPRI/PET/MRI images for analysis.

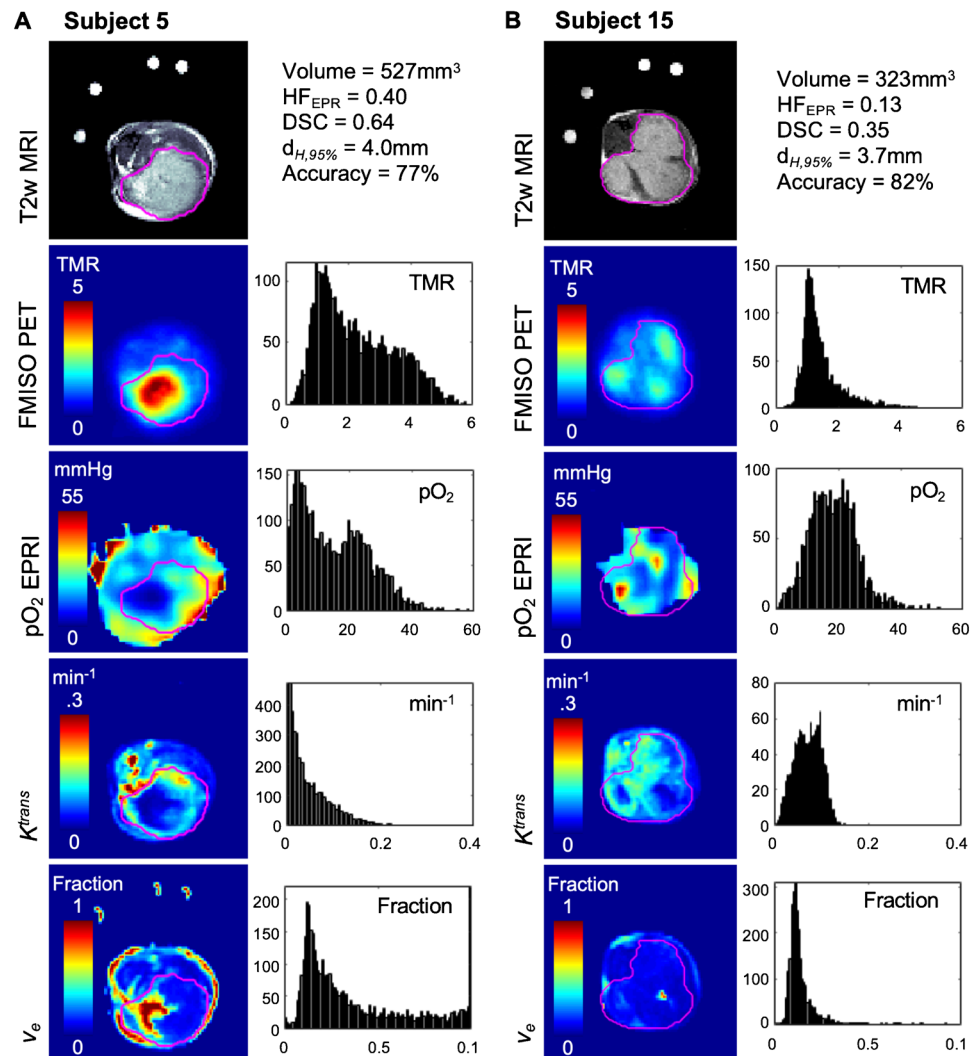
Optimal FMISO PET threshold to localize hypoxia

The optimal FMISO threshold to define hypoxia was determined by using EPRI as the reference truth for hypoxia, which is well-established as $pO_2 \leq 10$ mmHg [29]. Receiver operating characteristic (ROC) analysis [30] was repeated for different pO_2 thresholds ranging from 6 to 14 mmHg to confirm the EPRI $pO_2 \leq 10$ mmHg hypoxia threshold (Supplemental Figure S2). One-way analysis of variance (ANOVA) was used to compare means of the area under the curve (AUC) across all subjects for each EPR threshold.

FMISO-based hypoxia thresholds were defined by a variation of TMR and SUV thresholds commonly found in the literature [14–17]. Figure 2A shows a scatter plot from an example tumor's pO_2 and SUV voxel values, and how true-positive fractions (TPF) and false-positive fractions (FPF) change based on the FMISO uptake threshold. The TPF is the fraction of voxels within a tumor that FMISO PET accurately classified as hypoxic; the FPF is the fraction of tumor voxels that FMISO PET misclassified as hypoxic but were actually normoxic. PET thresholds were defined by $SUV \geq X$, where X ranges from 0 to 5. PET thresholds were further evaluated by $SUV \geq X \times SUV_{mean}$ or $SUV \geq X \times SUV_{median}$, and $SUV \geq Y \times SUV_{max}$ where Y ranges from 0 to 1. The SUV_{mean} , SUV_{median} , and SUV_{max} were calculated over all voxels in each tumor. Analysis was repeated for thresholds in TMR units.

Three metrics were used to define similarity between hypoxia in EPRI and FMISO PET: accuracy, dice similarity coefficient (DSC), and the 95th percentile Hausdorff distance ($d_{H,95\%}$). Accuracy was defined by the fraction of true positives (TP) and true negatives (TN) over the entire tumor including false positives (FP) and negatives (FN): $accuracy = (TP + TN) / (TP + TN + FP + FN)$. The $DSC = 2|X \cap Y| / (|X| + |Y|)$, where X and Y are hypoxic voxels defined by EPRI and PET respectively, is the ratio of the number of voxels in the overlapping region of hypoxia to the sum of the number of hypoxic voxels in each region. The $d_{H,95\%}$ measured the greatest distance from the nearest points in the EPRI-defined hypoxic region to the

Fig. 1 Axial slices in the center of the tumor and histogram distributions for **A** Mouse 5 with a large, compact hypoxic volume, and **B** Mouse 15 with a low, heterogeneous hypoxia distribution



PET-defined hypoxic region. The $d_{H,95\%}$ was normalized and subtracted from 1, denoted by $\|d_{H,95\%}\|$, so that all three metrics would range from 0 to 1 (lowest to highest similarity between the two hypoxic tumor subregions).

The overall hypoxic similarity (OHS) was calculated for each tumor as the mean of accuracy, DSC, and $\|d_{H,95\%}\|$, again ranging from 0 to 1. For all metrics, the mean across all tumors was plotted against each potential FMISO threshold (Fig. 3), setting true hypoxia at pO_2 EPRI ≤ 10 mmHg. The FMISO thresholds with maximum OHS were defined as the optimal FMISO threshold for TMR, TMR_{mean} , TMR_{median} , TMR_{max} , SUV , SUV_{mean} , SUV_{median} , and SUV_{max} . Additionally, the hypoxic fraction was calculated based on FMISO PET images (HF_{PET}) at thresholds with maximum OHS to compare to hypoxic fractions defined by EPRI (HF_{EPR}).

Correlations between EPRI, FMISO PET, and DCE-MRI

DCE-MRI parametric images of K^{trans} (contrast agent rate of transport to tissue) and v_e (volume fraction of the

extravascular extracellular space in tissue) were generated using the standard Tofts model [27]. Spearman correlation coefficients were calculated for each tumor between pO_2 EPRI, FMISO uptake, K^{trans} , and v_e to identify significant correlations between modalities. The paired t -test was used to compare inter-modality correlation strengths.

Validating *in vivo* images with H&E and IHC staining

Sectioned and stained slides were scanned with 40 \times resolution digital light field microscope and imported into CaseViewer and QuPath software for viewing. The H&E slide was manually registered to the T2-weighted axial MRI image that most closely resembled its anatomical features. Note the limitations of this method in registering *ex vivo* to *in vivo* samples due to tearing and deformation of the excised tissue. Regions of necrosis were identified by H&E, HIF-1 α expression in the cell nucleus, and CD31 staining of endothelial cells in sister sections, with guidance from a pathologist. Those regions were then identified in associated *in vivo* slices to see if (1) necrotic regions

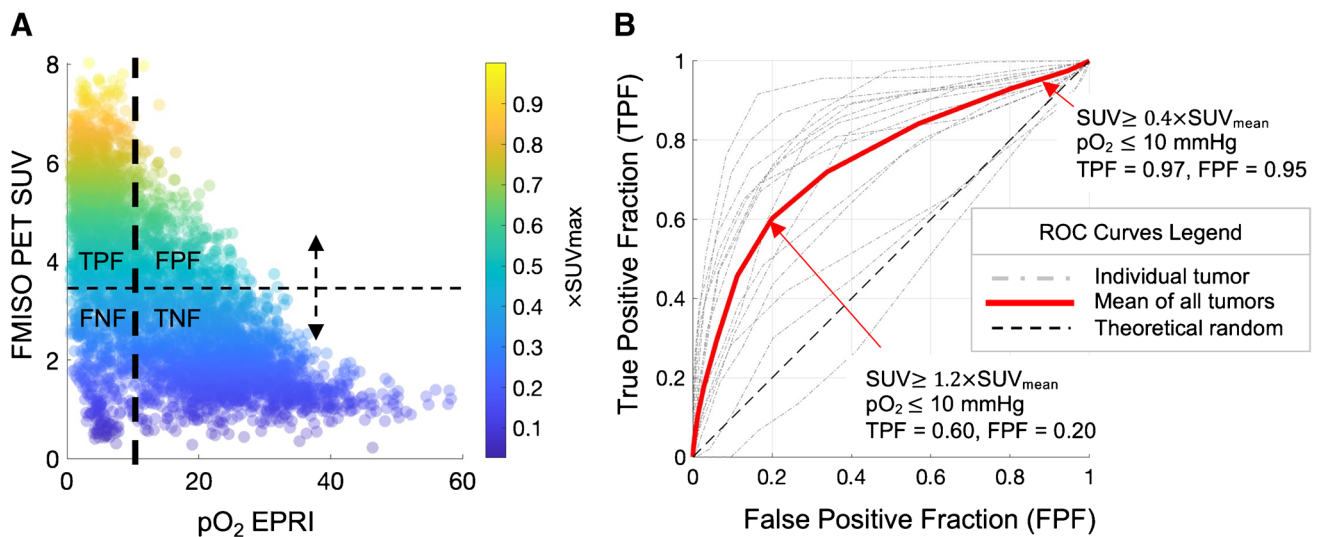
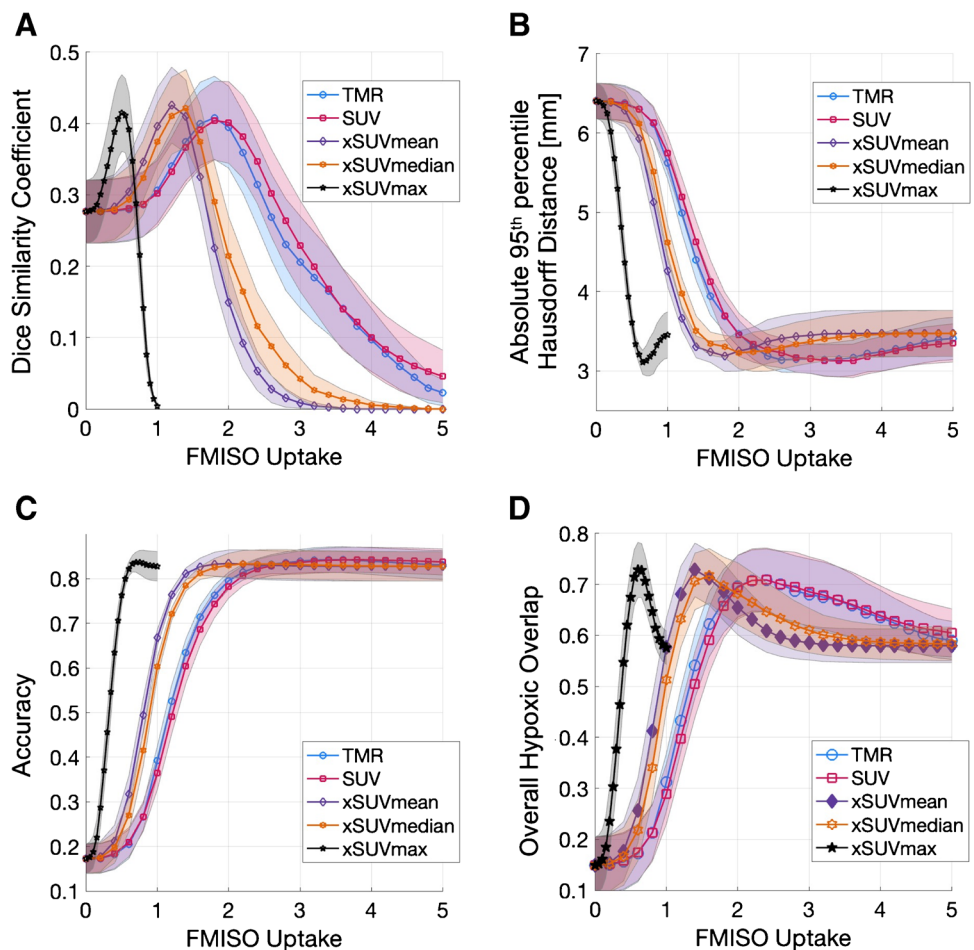


Fig. 2 **A** Scatterplot of tumor voxel values where hypoxia is defined by $pO_2 \leq 10$ mmHg (vertical dashed line) and FMISO PET threshold for hypoxia is exploratory (horizontal dashed line). The true-positive fraction (TPF) and false-positive fraction (FPF) vary by the FMISO threshold for hypoxia. **B** Example ROC curves (red) from result of sweeping through scaled FMISO \times SUV_{mean} thresholds from 0 to 5.

Dotted-dashed grey lines show ROC curves for individual tumors with area under the curve (AUC) ranging from 0.42 to 0.92. The thick red ROC curve shows mean ROC curve (AUC=0.74) across all tumors for each FMISO threshold. The dashed black line shows the theoretical random ROC curve (AUC=0.5) where TPF=FPF

Fig. 3 Tumor hypoxia overlap between PET/EPRI for select FMISO PET uptake units: TMR, SUV, \times SUV_{mean}, \times SUV_{median}, and \times SUV_{max}. Mean, median, and maximum TMR images generated identical results, so are excluded from the figure. Shaded curves show mean and standard error across all tumors. For each unit, the **A** DSC, **B** $d_{H,95\%}$, and **C** accuracy is displayed for all potential FMISO PET thresholds. **D** $OHS = (DSC + \|d_{H,95\%}\| + Acc)/3$ identifies the peak thresholds where FMISO uptake best overlaps with EPRI-defined $pO_2 \leq 10$ mmHg (specified in Table 1)



corresponded to areas of low K^{trans} and high v_e , (2) areas without CD31 stains corresponded to hypoxia, and (3) HIF-1 α expression corresponded to hypoxia.

Results

Figure 1 shows two examples of tumors (in all modalities) selected to show variation in hypoxic fraction, FMISO uptake, and tumor volume. For example, Mouse 5 in Fig. 1A had a large tumor volume and hypoxic core, while Mouse 15 in Fig. 1B had a small tumor volume with several nodules and a heterogeneous spread of hypoxia.

Optimal FMISO PET threshold to localize hypoxia

The mean OHS reached its peak with hypoxia defined by FMISO SUV $\geq 1.4 \times \text{SUV}_{\text{mean}}$ and SUV $\geq 0.6 \times \text{SUV}_{\text{max}}$ (and the same for TMR). Figure 3 shows the distribution of DSC, $d_{H,95\%}$, accuracy, and OHS at all potential FMISO uptake thresholds. Table 1 shows the resulting DSC, $d_{H,95\%}$, and accuracy values at each unit's maximum OHS values: SUV ≥ 2.4 , SUV $\geq 1.6 \times \text{SUV}_{\text{median}}$, SUV $\geq 1.4 \times \text{SUV}_{\text{mean}}$, and SUV $\geq 0.6 \times \text{SUV}_{\text{max}}$.

The mean and standard deviation of the AUC for ROC curves across all mice was 0.74 ± 0.1 for EPRI $pO_2 \leq 10$ mmHg. Using a lower threshold of $pO_2 \leq 6$ mmHg had a lower AUC (0.70 ± 0.2), but there was no significant difference in results across pO_2 thresholds ($p=0.9$). ROC curves and AUC values are displayed in Supplemental Figure S2.

Box plot distributions of HF_{EPRI} and HF_{PET} are shown in Fig. 4A. Three-dimensional masks of tumor hypoxia with different FMISO thresholds are shown in Fig. 4B. This visualization demonstrates using an absolute threshold of TMR or SUV to define hypoxia, rather than a scaled threshold such as SUV_{mean} ,

risks underestimating hypoxia. This would be detrimental to a radiation treatment plan since a large portion of hypoxic clonogenic cells may survive.

Correlations between EPRI, FMISO PET, and DCE-MRI

Table 2 shows median (top right) and min/max (bottom left) monotonic Spearman correlation coefficients between tumor voxels of pO_2 , FMISO uptake, K^{trans} , and v_e , which were calculated for each mouse. Figure 5 shows the histogram distributions of correlation strengths between pO_2 with FMISO uptake (5A), pO_2 and FMISO uptake with K^{trans} (5B), and v_e (5C). Moderate correlations ($p < 0.05$) were observed between pO_2 with FMISO uptake and K^{trans} with FMISO uptake. Only weak correlations were observed with v_e .

Negative correlations were observed between all pO_2 vs FMISO voxel values ($\rho_{\text{median}} = -0.52$, $p < 0.001$ and $\rho_{\text{min}} = -0.71$, $p < 0.001$), confirming low pO_2 in tumor subregions with high FMISO uptake. Positive correlations between pO_2 vs K^{trans} ($\rho_{\text{median}} = 0.33$, $p < 0.001$, $\rho_{\text{max}} = 0.58$, $p < 0.001$) support the theory that higher vascular perfusion and permeability increases with pO_2 . Negative correlations between FMISO uptake vs K^{trans} ($\rho_{\text{median}} = -0.41$, $p < 0.001$, $\rho_{\text{min}} = -0.66$, $p < 0.001$) support that vascular perfusion and permeability decreases while FMISO uptake increases.

The paired t -test comparing strength of correlations showed a significantly higher strength of absolute ρ for FMISO uptake vs K^{trans} ($|\rho_{\text{mean}}| = 0.34$) than for pO_2 vs K^{trans} ($|\rho_{\text{mean}}| = 0.28$) ($p = 0.018$). However, both mean correlations were generally weak.

Validating *in vivo* images with H&E and IHC staining

Regions with low K^{trans} and high v_e and hypoxia in both FMISO PET and EPRI corresponded with regions of

Table 1 A summary of mean \pm standard deviation values of DSC, $d_{H,95\%}$, accuracy, OHS, and HF_{PET} over all mice for each FMISO uptake unit when compared to the reference $pO_2 \leq 10$ mmHg hypoxia

| | TMR ≥ 2.4 | SUV ≥ 2.4 | $\geq 1.4 \times \text{SUV}_{\text{mean}}$ | $\geq 1.6 \times \text{SUV}_{\text{median}}$ | $\geq 0.6 \times \text{SUV}_{\text{max}}$ |
|-------------------|----------------|----------------|--|--|---|
| DSC | 0.31 \pm .2 | 0.35 \pm .2 | 0.41 \pm .2 | 0.37 \pm .2 | 0.39 \pm .2 |
| $d_{H,95\%}$ [mm] | 3.3 \pm .6 | 3.3 \pm .8 | 3.3 \pm .5 | 3.3 \pm .6 | 3.2 \pm .4 |
| Accuracy | 0.82 \pm .07 | 0.82 \pm .08 | 0.81 \pm .05 | 0.81 \pm .06 | 0.82 \pm .06 |
| OHS | 0.708 \pm .2 | 0.709 \pm .2 | 0.728 \pm .2 | 0.717 \pm .2 | 0.728 \pm .2 |
| HF_{PET} | 0.14 \pm .1 | 0.21 \pm .2 | 0.18 \pm .05 | 0.16 \pm .07 | 0.16 \pm .07 |

DSC = dice similarity coefficient

$d_{H,95\%}$ = Hausdorff distance (95th percentile)

OHS = Overall hypoxia similarity

HF_{PET} = Hypoxic fraction defined by FMISO PET

HF_{EPRI} = Hypoxic fraction defined by pO_2 EPRI

TMR = Tumor-to-muscle ratio

SUV = Standardized uptake value

definition from EPRI, where mean $HF_{\text{EPRI}} = 0.17 \pm 0.2$. The displayed FMISO TMR and SUV hypoxia thresholds shown in this table had the highest OHS values

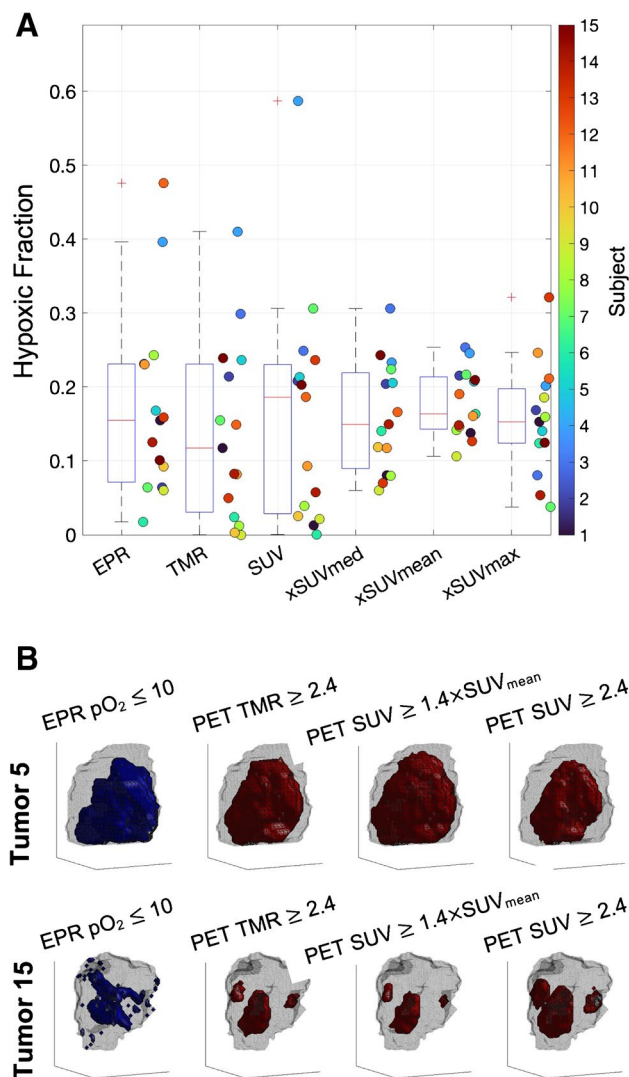


Fig. 4 **A** Comparison of hypoxic fractions HF_{EPR} and HF_{PET} at TMR ≥ 2.4 , SUV ≥ 2.4 , SUV $\geq 1.6 \times SUV_{median}$, SUV $\geq 1.4 \times SUV_{mean}$, and SUV $\geq 0.6 \times SUV_{max}$. Markers show individual hypoxic fraction (HF) values next to their respective boxplots. Because the mean, median, and max TMR HF distributions were identical to SUV, they were excluded from the plot. There is no statistical difference in the means (using ANOVA, $p=0.66$) of HF values across thresholds. However, there is a significant difference in the variance between the “true” HF from EPR to HF defined by SUV_{median} ($p=0.02$), SUV_{mean} ($p<0.001$), and SUV_{max} ($p=0.02$). **B** Examples of tumor hypoxia defined by pO₂ EPRI (blue) vs FMISO PET (red) using various optimal thresholds for Tumor 5 and Tumor 15 (axial slices shown in Fig. 1)

necrosis and no stained blood vessels with CD31 (Fig. 6A, red arrows). Tumor regions without apparent necrosis and stained blood vessels with CD31 (Fig. 6B, green arrows) corresponded with oxygenated tumor regions (high pO₂ and low FMISO uptake). HIF-1 α expression in tumor cell nuclei was apparent throughout the entire tumor, particularly at

tumor edges and around new vascular growth. There was no HIF-1 α expression in healthy muscle cells.

Discussion

We have calculated the optimal threshold to apply to a late static FMISO PET image 2 h post-injection. Other groups have published more complete dynamic imaging and kinetic analysis that would require a longer PET scan over several hours and more complex image processing and compartmental data analysis [31, 32]. However, a simple approach is necessary for hypoxia imaging to be widely implemented, which is the goal of this work.

The importance of using the optimal FMISO threshold in locating tumor hypoxia is in the risk of a too-high FMISO threshold, which could underestimate hypoxia with negative treatment outcomes. Small fractions of missed hypoxia in radiation treatment can still result in clonogenic hypoxic tumor cells resulting in clinical failure as discussed in Epel et al. [4]. This must be balanced by the risk of overestimating tumor hypoxia with an FMISO threshold that is too low, which could result in over-treating a tumor and organs at risk.

Results of our study confirmed that overall hypoxic similarity between FMISO PET/EPRI images were maximized at similar FMISO thresholds as reported by independent research groups [14–20] of SUV $\geq 1.4 \times SUV_{mean}$ and SUV $\geq 0.6 \times SUV_{max}$, and the same with TMR units. However, SUV may be more appropriate than TMR because units of SUV do not require a subjective contour of a muscle ROI.

The DSC and $d_{H,95\%}$ were dependent on the tumor’s hypoxic fraction, where larger hypoxic fractions had higher DSC values (indicating better overlap) but also higher $d_{H,95\%}$ values (indicating worse overlap), shown in Supplemental Figure S3. This tradeoff supports the need for multiple metrics to define the quality of overlap between hypoxic tumor subregions shown in pO₂ EPRI vs FMISO PET.

Vera’s Phase II study [14] used an FMISO PET threshold of SUV ≥ 1.4 to define hypoxic lesions to deliver a boost dose to, where 48% of the cohort’s tumor histology was lung squamous cell carcinomas. The study showed that FMISO uptake was strongly associated with poor prognosis features, but delivering a boost dose to the hypoxic subregions did not reverse those features. A possibility of why this was observed was a suboptimal choice of threshold to define hypoxia with FMISO. For example, when using the threshold SUV ≥ 1.4 in this study’s dataset, the mean \pm standard deviation of the DSC was 0.38 ± 0.2 and $d_{H,95\%}$ was 9.2 ± 2 mm. The $d_{H,95\%}$ increased by almost 6 mm compared to the use of a more optimal threshold like SUV $\geq 1.4 \times SUV_{mean}$. This large discrepancy between definitions of hypoxic tumor regions could result in suboptimal boost targets for treatment, which affects patient outcome.

Fig. 5 Histograms of Spearman correlation coefficients between tumor hypoxia (pO_2 EPRI and FMISO SUV) with vascular permeability/perfusion (K^{trans}) and fraction of extracellular-extravascular space (v_e) for each tumor. **A** Negative correlations are consistent between FMISO SUV and EPRI pO_2 . **B** Negative weak correlations between FMISO SUV and K^{trans} (pink) and positive weak correlations between EPRI pO_2 with K^{trans} (cyan). **C** Positive weak correlations between FMISO SUV and v_e (pink) and negative weak correlations between EPRI pO_2 with v_e (cyan)

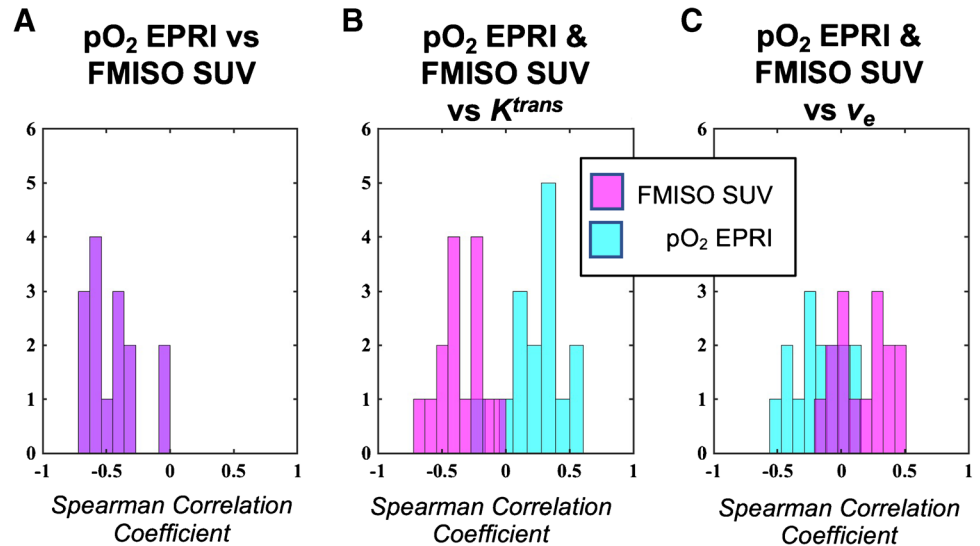


Table 2 Spearman correlation coefficients ρ between all *in vivo* modalities. Median ρ values are on the right above the diagonal in a darker shade of gray. The minimum and maximum ρ values are on the

left below the diagonal in a lighter shade of gray. Top values show maximum ρ ; bottom values show minimum ρ .

| | EPR pO_2 | FMISO SUV | DCE-MRI K^{trans} | DCE-MRI v_e |
|------------------------|------------------------|---------------------|------------------------|------------------|
| EPR pO_2 | 1 | -0.52*** | 0.33*** | -0.19*** |
| FMISO SUV | -0.0042*** -0.71*** | 1 | -0.41*** | 0.15*** |
| DCE-MRI K^{trans} | 0.58 -0.18*** | -0.0016 -0.66*** | 1 | -0.20*** |
| DCE-MRI v_e | 0.15 -0.50*** | 0.48 -0.14*** | 0.16 -0.64*** | 1 |

Associated p values are shown by asterisks: * = $p \leq 0.05$, ** = $p \leq 0.01$, *** = $p < 0.001$

The resolution differences between preclinical EPR and PET imaging modalities were < 1 mm. Previously evaluated resolutions of this study's imaging systems were found to be ~ 1.6 mm for PET and ~ 1.0 mm for EPROI [23]. All multimodal tumor images were resampled to isotropic 0.5 mm output voxel resolution of the PET image, so EPR pO_2 images were upsampled from their 0.67 mm isotropic resolution. The effect of resampling would mostly affect similarity metrics at the edges of hypoxic tumor subregions, which straddle each threshold to define hypoxia. This did not significantly affect the AUC for various EPR pO_2 thresholds of hypoxia ($p > 0.05$). DCE-MRI images of K^{trans} and v_e were downsampled from $0.1 \times 0.1 \times 0.75$ mm³, which would have more strongly affected statistical analysis and accuracy of similarity metrics in the axial plane in tumors with more heterogeneous vascular perfusion and permeability features.

This may be a contributing factor to the generally weak-to-moderate strengths of Spearman correlations.

Generally weak to moderate correlations between EPR/PET hypoxia images with DCE-MRI parametric images support that tumor hypoxia is a much more complex process than vascular supply [33]. Recent work by Hillestad et al. [27] shows that a combination of K^{trans} and v_e (rather than K^{trans} and v_e alone) can be used to predict hypoxia level and hypoxic fraction. That in turn predicted progression-free survival using hypoxic fraction and K^{trans} values, but not v_e . This is consistent with our results showing some moderately strong correlations between pO_2 with K^{trans} , but no correlations between pO_2 with v_e . The stronger correlations between FMISO uptake with K^{trans} compared to pO_2 with K^{trans} suggest that FMISO is more susceptible to effects of vascular perfusion and permeability than EPRI.

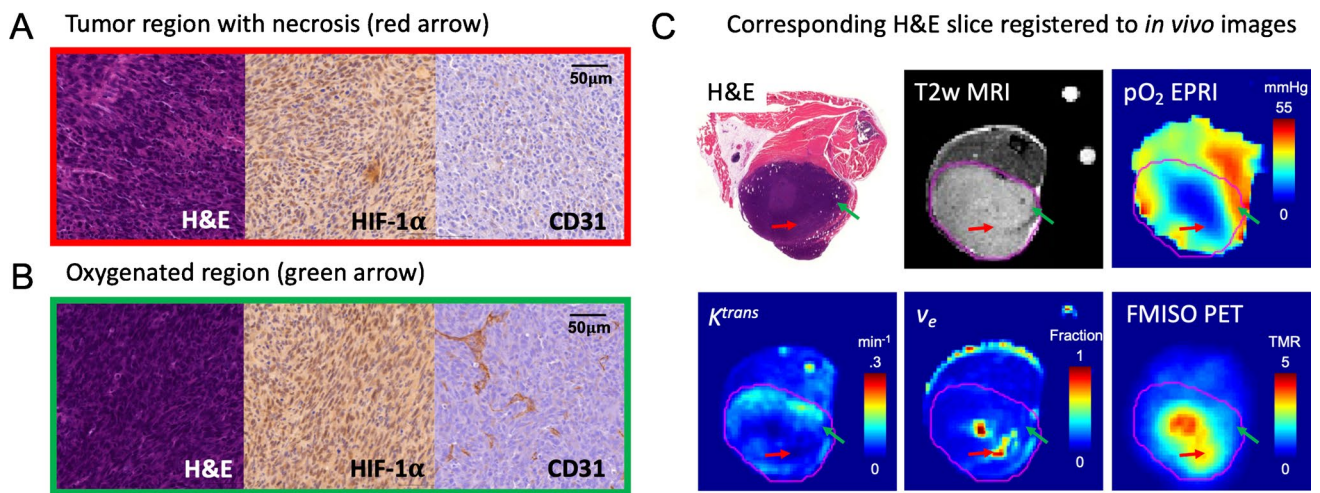


Fig. 6 Magnified H&E and immunohistological stains of HIF-1 α and CD31 expression in hypoxic tumor cells regions with some necrosis (A, D) and tumor region without apparent hypoxia (B, E). Cor-

responding *in vivo* axial slices with the registered H&E slide (C, F) show corresponding red arrows (necrosis/hypoxia) and green arrows (oxygenated tumor cells)

HIF-1 α expression was not localized only to hypoxic tumor regions, but throughout the whole tumor, with darker nucleic stains around blood vessels stained with CD31. This supports that in the presence of hypoxia, and surrounding necrosis, HIF-1 α induces angiogenesis [34, 35]. We initially considered there was overstaining, but there was no HIF-1 α expression in healthy muscle cells. Tumor regions without CD31 staining, i.e., regions without blood-delivering vasculature, were more strongly associated with necrosis and low K^{trans} .

While these results were consistent throughout the two tumors for which H&E and IHC staining was completed, a limitation to the study is that only two tumors were used. However, those tumors are representative of the whole group: Tumor 14 had a hypoxic core with high similarity between FMISO PET/EPROI-defined hypoxia and high FMISO uptake, while Tumor 15 had a heterogeneous spread of hypoxia with low similarity between FMISO PET/EPROI-defined hypoxia and low FMISO uptake.

Another limitation to our study is the lack of radiation treatment outcome results when delivering boost doses to these optimally defined hypoxic tumor subregions imaged with FMISO PET. However, this is the only *in vivo* study to use EPRI as the ground truth for tumor hypoxia, and the validity of using EPRI to define and treat hypoxia has been previously verified and published [4, 24]. Our optimal threshold for defining hypoxia with FMISO PET falls within the range of clinical studies using FMISO to locate tumor hypoxia for radiation boosts [8–16]. Ongoing experiments will carry out preclinical *in vivo* tumor hypoxia boost studies and will be reported in the future.

The presented analysis was performed in a single animal tumor model system. The results are liable to change

in other tumor models that may be more likely to develop severe necrosis, stromal structures, and different patterns of vascularization. For example, similar work in clinical studies have shown different kinetics in FMISO PET and DCE-MRI in head-and-neck cancer [36] compared to breast cancer [37] patients. To address this concern, work is ongoing to repeat our study in mammary adenocarcinomas and fibrosarcomas preclinical mouse models.

The generally low DSC and high $d_{H,95\%}$ values show the need for a potential correction to FMISO PET images using DCE-MRI, but this study aims to identify the optimal FMISO PET threshold for clinical settings where only static FMISO PET imaging is feasible. Repeating the study in other tumor types will identify potential differences or similarities between tumor physiology and hypoxia across tumor models that may exhibit a different volume of distribution, which may affect the pO₂ EPRI vs FMISO PET correlations, thereby altering the optimum threshold setting.

Conclusion

This is the first *in vivo* comparison of FMISO uptake with pO₂ EPRI in preclinical squamous cell carcinomas to identify the optimal thresholds to define tumor hypoxia ($SUV \geq 1.4 \times SUV_{mean}$ and $SUV \geq 0.6 \times SUV_{max}$). A hybrid PET/EPRI imager was used to ensure identical physiological conditions of the mouse during imaging. Over all tumors, the relatively low mean DSC and high $d_{H,95\%}$ suggest the need to apply a correction to FMISO PET images, for which work is ongoing [26].

Supplementary Information The online version contains supplementary material available at <https://doi.org/10.1007/s00259-022-05889-4>.

Acknowledgements We would like to thank the University of Chicago's Cyclotron Facility, the Integrated Small Animal Imaging Research Resource, and the Human Tissue Resource Center. We would also like to thank Dr. Scott Trinkle for his helpful comments after reading over the manuscript, Dr. Nicole Cipriani's expertise in pathology, and Dr. Hannah Zhang's advice in early histological imaging sample preparation.

Author contribution The following authors contributed to acquiring data: Inna Gertsenshteyn, Boris Epel, Eugene Barth, John Lukens, Xiaobing Fan, Hsui-Ming Tsai, Lara Leoni, Heejong Kim, Marta Zamora, Erica Markiewicz, Subramanian Sundramoorthy, Richard Freifelder, Mohammed Bhuiyan, and Anna Kucharski. The following authors contributed to the conception and design of the data: Inna Gertsenshteyn, Boris Epel, Brian Roman, Gregory Karczmar, Chien-Min Kao, Howard Halpern, Chin-Tu Chen. The following authors contributed to analyzing and interpreting data: Inna Gertsenshteyn, Amandeep Ahluwalia, Mihai Giurcanu, Brian Roman, Gregory Karczmar, Howard Halpern, Chin-Tu Chen. The first draft of the manuscript was written by Inna Gertsenshteyn, and all authors commented on previous versions of the manuscript. All authors read and approved the final manuscript.

Funding This study was funded by National Institutes of Health grants R01 CA098575, R01 CA 236385, P30 CA014599, P41 EB002034, F31 CA254223, S10 OD025265, and R01 EB029948.

Data availability The datasets generated during and/or analyzed during the current study are available from the first author or corresponding author on reasonable request.

Declarations

Ethics approval All applicable international, national, and/or institutional guidelines for the care and use of animals were followed. This article does not contain any studies with human participants performed by any of the authors.

Conflict of interest Author Chin-Tu Chen (CTC) is a PI for the following grants from NIH/NIBIB (R01 EB022388 and R01 EB029948), NIH/NIDA (R01 DA044760), and NIH/NCI (P30 CA14599 facility). CTC receives a personal fee from the American Institute of Physics for editorial responsibilities. Other relationships include institute licenses patents (CTC is a co-inventor) to RefleXion Medical, Inc. and Incom. CTC is a co-founder and on the board of directors of EVO Worldwide LLC and AEPX Imaging, Inc. Author Howard Halpern (HH) is a PI for the following grants from NIH/NCI (R01 CA098575 and P30 CA014599) and NIH/NIBIB (P41 EB002034). HH also holds two US patents (8,664,955 and 9,392,957) to him and one (9,392,957) to author Boris Epel (BE) for aspects of the pO₂ imaging technology; HH and BE are also members of a start-up company O2M to market the pO₂ imaging technology in preclinical models. No other potential conflicts of interest relevant to this article exist. The rest of the authors have no relevant financial or non-financial interests to disclose.

References

- Hockel M, Vaupel P. Tumor hypoxia: definitions and current clinical, biologic, and molecular aspects. *J Natl Cancer Inst.* 2001;93(4):266–76.
- Vaupel P, Mayer A. Hypoxia in cancer: significance and impact on clinical outcome. *Cancer Metastasis Rev.* 2007;26(2):225–39.
- Overgaard J. Hypoxic radiosensitization: adored and ignored. *J Clin Oncol.* 2007;25(26):4066–74.
- Epel B, Maggio MC, Barth ED, et al. Oxygen-guided radiation therapy. *Int J Radiat Oncol Biol Phys.* 2019;103(4):977–84.
- Dewhirst MW. Relationships between cycling hypoxia, HIF-1, angiogenesis and oxidative stress. *Radiat Res.* 2009;172(6):653–65.
- Muz B, Azab F, Azab AK. The role of hypoxia in cancer progression, angiogenesis, metastasis, and resistance to therapy. *Hypoxia (Auckl).* 2015;3:83–92.
- Schwarz G. Über Desensibilisierung gegen Röntgen- und Radiumstrahlen. *Munch Med Wochenschr.* 1909;56:1217–8.
- Crabtree HG, Cramer W. The action of radium on cancer cells II - some factors determining the susceptibility of cancer cells to radium. *Proc R Soc Lond B.* 1933;113(782):238–50.
- Thomlinson RH, Gray LH. The histological structure of some human lung cancers and the possible implications for radiotherapy. *Br J Cancer.* 1955;9:539–63.
- Kishimoto S, Saito K, Enomoto A, et al. Pulsed electron paramagnetic resonance imaging: applications in the studies of tumor physiology. *Antioxid Redox Signal.* 2018;28(15):1378–93.
- Epel B, Redler G, Tormyshev V, Halpern HJ. Towards human oxygen images with electron paramagnetic resonance imaging. *Adv Exp Med Biol.* 2016;876:363–9.
- Krohn KA, Link JM, Mason RP. Molecular imaging of hypoxia. *J Nucl Med.* 2008;49(Suppl 2):129S-S148.
- Lopci E, Grassi I, Chiti A, et al. PET radiopharmaceuticals for imaging of tumor hypoxia: a review of the evidence. *Am J Nucl Med Mol Imaging.* 2014;4:365–84.
- Vera P, Thureau S, Chaumet-Riffaud P, et al. Phase II Study of a radiotherapy total dose increase in hypoxic lesions identified by 18F-misonidazole PET/CT in patients with non-small cell lung carcinoma (RTEP5 study). *J Nucl Med.* 2017;58(7):1045–53.
- Riaz N, Sherman E, Pei X, et al. Precision radiotherapy: reduction in radiation for oropharyngeal cancer in the 30 ROC Trial. *J Natl Cancer Inst.* 2021;113(6):742–51.
- Fleming IN, Manavaki R, Blower PJ, et al. Imaging tumour hypoxia with positron emission tomography. *Br J Cancer.* 2015;112(2):238–50.
- Ferini G, Valenti V, Tripoli A, et al. Lattice or oxygen-guided radiotherapy: what if they converge? Possible future directions in the era of immunotherapy. *Cancers (Basel).* 2021;13(13):3290.
- Lindblom E, Dasu A, Uhrdin J, et al. Defining the hypoxic target volume based on positron emission tomography for image guided radiotherapy - the influence of the choice of the reference region and conversion function. *Acta Oncol.* 2017;56(6):819–25.
- Chang JH, Wada M, Anderson NJ, et al. Hypoxia-targeted radiotherapy dose painting for head and neck cancer using (18)F-FMISO PET: a biological modeling study. *Acta Oncol.* 2013;52(8):1723–9.
- de Figueiredo HB, Zacharatos C, Galland-Girodet S, et al. Hypoxia imaging with [18F]-FMISO-PET for guided dose escalation with intensity-modulated radiotherapy in head-and-neck cancers. *Strahlenther Onkol.* 2015;191(3):217–24.
- Hendrickson K, Phillips M, Smith W, Peterson L, Krohn K, Rajendran J. Hypoxia imaging with [F-18] FMISO-PET in head and neck cancer: potential for guiding intensity modulated radiation therapy in overcoming hypoxia-induced treatment resistance. *Radiother Oncol.* 2011;101(3):369–75.
- Dewhirst MW, Cao YT, Moeller B. Cycling hypoxia and free radicals regulate angiogenesis and radiotherapy response. *Nat Rev Cancer.* 2008;8(6):425–37.
- Kim H, Epel B, Sundramoorthy S, et al. Development of a PET/EPRI combined imaging system for assessing tumor hypoxia. *J Instrum.* 2021;16(P03031). <https://doi.org/10.1088/1748-0221/16/03/p03031>.

24. Elas M, Bell R, Hleihel D, et al. Electron paramagnetic resonance oxygen image hypoxic fraction plus radiation dose strongly correlates with tumor cure in F5a fibrosarcomas. *Int J Radiat Oncol Biol Phys.* 2008;71(2):542–9.
25. Lim JL, Berridge MS. An efficient radiosynthesis of [¹⁸F]fluoromisonidazole. *Appl Radiat Isot.* 1993;44(8):1085–91.
26. Gertsenshteyn I, Epel B, Barth E, et al. Improving tumor hypoxia location in ¹⁸F-misonidazole PET with dynamic contrast-enhanced MRI using quantitative electron paramagnetic resonance partial oxygen pressure images. *Radiol Imaging Cancer.* 2021;3(2):e200104. <https://doi.org/10.1148/rycan.2021200104>.
27. Tofts PS, Brix G, Buckley DL, et al. Estimating kinetic parameters from dynamic contrast-enhanced T1-weighted MRI of a diffusible tracer: standardized quantities and symbols. *J Magn Reson Imaging.* 1999;10:223–32.
28. Epel B, Halpern HJ. EPR oxygen imaging workflow with MATLAB Image Registration Toolbox. *Appl Magn Reson.* 2021;52(10):1311–9.
29. Gertsenshteyn I, Giurcanu M, Vaupel P, Halpern H. Biological validation of electron paramagnetic resonance (EPR) image oxygen thresholds in tissue. *J Physiol.* 2021;599(6):1759–67.
30. Metz CE. Basic principles of ROC analysis. *Semin Nucl Med.* 1978;8(4):283–98.
31. Grkovski M, Schöder H, Lee N, et al. Multiparametric imaging of tumor hypoxia and perfusion with ¹⁸F-fluoromisonidazole dynamic PET in head and neck cancer. *J Nucl Med.* 2017;58(7):1072–80.
32. Thorwarth D, Eschmann SM, Paulsen F, Alber M. A kinetic model for ¹⁸F-Fmiso PET data to analyse tumour hypoxia. *Phys Med Biol.* 2005;50(10):2209–24.
33. Horsman MR, Vaupel P. Pathophysiological basis for the formation of the tumor microenvironment. *Front Oncol.* 2016;6(66). <https://doi.org/10.3389/fonc.2016.00066>.
34. Krock B, Skuli N, Simon CM. Hypoxia-induced angiogenesis: good and evil. *Genes Cancer.* 2011;2(12):1117–33.
35. Karth J, Ferrer FA, Perman E, et al. Coexpression of hypoxia-inducible factor 1- α and vascular endothelial growth factor in Wilms' tumor. *J Pediatr Surg.* 2000;35(12):1749–53.
36. Simoncic U, Leibfarth S, Welz S, et al. Comparison of DCE-MRI kinetic parameters and FMISO-PET uptake parameters in head and neck cancer patients. *Med Phys.* 2017;44(6):2358–68.
37. Carmona-Bozo JC, Manavaki R, Woitek R, et al. Hypoxia and perfusion in breast cancer: simultaneous assessment using PET/MR imaging. *Eur Radiol.* 2021;31(1):333–44.

Publisher's note Springer Nature remains neutral with regard to jurisdictional claims in published maps and institutional affiliations.